Published in
Boundary-Layer Meteorology 135, issue 2, 313-331, 2010
which should be used for any reference to this work

Frequency of Boundary-Layer-Top Fluctuations in Convective and Stable Conditions Using Laser Remote Sensing

Giovanni Martucci · Renaud Matthey · Valentin Mitev · Hans Richner

Abstract The planetary boundary-layer (PBL) height is determined with high temporal and altitude resolution from lidar backscatter profiles. Then, the frequencies of daytime thermal updrafts and downdrafts and of nighttime gravity waves are obtained applying a fast Fourier transform on the temporal fluctuation of the PBL height. The principal frequency components of each spectrum are related to the dominant processes occurring at the daytime and nighttime PBL top. Two groups of cases are selected for the study: one group combines daytime cases, measured in weak horizontal wind conditions and dominated by convection. The cases show higher updraft and downdraft frequencies for the shallow, convective boundary layer and lower frequencies for a deep PBL. For cases characterized by strong horizontal winds, the frequencies directly depend on the wind speed. The temporal variation of the PBL height is determined also in the likely presence of lee waves. For nighttime cases, the main frequency components in the spectra do not show a real correlation with the nocturnal PBL height. Altitude fluctuations of the top of the nocturnal boundary layer are observed even though the boundary layer is statically stable. These oscillations are associated with the wind shear effect and with buoyancy waves at the PBL top.

Giovanni Martucci and Renaud Matthey—formerly at Observatory of Neuchâtel, Rue de l'Observatoire 58, CH-2002, Neuchâtel, Switzerland.

G. Martucci (✉)
School of Physics & Centre for Climate and Air Pollution Studies, Environmental Change Institute, National University of Ireland, Galway, Galway, Ireland
e-mail: giovanni.martucci@nuigalway.ie

R. Matthey
Laboratory for Time and Frequency, Institute of Physics, University of Neuchâtel, 2000 Neuchâtel, Switzerland

V. Mitev
CSEM – Centre Suisse d'électronique et de Microtechnique, Rue Jaquet-Droz 1, 2002 Neuchâtel, Switzerland
e-mail: valentin.mitev@csem.ch

H. Richner
Institute for Atmospheric and Climate Science, ETH Hönggerberg HPP, 8093 Zurich, Switzerland

Keywords Convection · Lidar · Planetary boundary-layer height · Thermals · Top oscillation

Abbreviations

PBL	Planetary boundary layer
CBL	Convective boundary layer
EARLINET	European Aerosol Research Lidar Network
EC	European Commission
EZ	Entrainment zone
FFT	Fast Fourier transform
FOV	Field of View
GS	Gradient signal
KH	Kelvin–Helmholtz
NBL	Nocturnal boundary layer
RCS	Range-corrected signal
SNR	Signal-to-noise ratio
UTC	Universal Coordinated Time
Var	Variance

1 Introduction

The planetary boundary layer (PBL) height and the entrainment-zone (EZ) thickness characterize the aerosol stratification in the lower troposphere (Stull 1988; Garratt 1992; McIlveen 1992; Steyn et al. 1999). The convective boundary-layer (CBL) height affects the vertical mixing of atmospheric constituents (Siebert et al. 2001), i.e. gases, aerosols and water vapour. Preceding studies (Neu et al. 1994; Beyrich and Gryning 1997; Flamant et al. 1997) investigated mechanisms leading to the mixing of air within the EZ, developing methods to determine the depth and the temporal fluctuation of this zone. Changes in the vertical and horizontal EZ structure significantly affect the near-surface pollution trade-off. The updrafts and downdrafts within the CBL represent the primary means by which the heat, moisture, momentum, and pollutants are transported between the earth's surface and the free troposphere. The precise reconstruction of the PBL convection is then critical to several boundary layer processes, (i) The latent heat flux initiated at the air–sea interface contributes to the process of convective clouds formation at the top of the marine boundary layer; (ii) Emission rates (both biogenic and anthropogenic) within the boundary layer can be assessed by monitoring their mixing at the boundary-layer top. Both (i) and (ii) are difficult to reproduce in numerical weather prediction models due to the coarse model spatial resolution compared to the scales at which these processes occur. Numerical models need then detailed, high resolution data assimilation in order to reproduce accurately such processes (De Wekker et al. 1997; Rampanelli and Zardi 2004; Zampieri 2005).

During the night the amount of mixing within the PBL and the exchange of air with the overlying free troposphere are considerably reduced. Turbulent motions within the nocturnal boundary layer (NBL) can occur in short, but intense, bursts. The low-level flow is often decoupled from the flow aloft within the low-level jet. When the vertical shear of the wind

is large, instability arises in the form of Kelvin–Helmholtz (KH) waves: it appears that the onset of KH instability occurs when the (gradient) Richardson number is smaller than a critical value $R_c = 0.25$. The NBL top often corresponds to the level where this condition is achieved.

Previous studies showed that the aerosol stratification through the PBL observed by lidar corresponds to the temperature stratification observed by radiosonde measurements, i.e., the lidar measurements can provide trustworthy PBL height (Menut et al. 1999; Sicard et al. 2006; Hennemuth and Lammert 2006; Lammert and Bösenberg 2006; Wiegner et al. 2006; Martucci et al. 2007). Knowledge of the PBL height with high temporal and altitude resolution allows the detection of fine features in the temporal fluctuation of the interface between the PBL and the free troposphere. At the same time, high resolution lidar measurements lead also to an increased noise component of the lidar signal itself and eventually to low signal-to-noise ratio (SNR). The optimization of the SNR allows determination of the vertical changes of the PBL height on a temporal scale of few minutes.

Steyn et al. (1998) and Hägeli (1998) proposed a lidar-based method to identify the PBL height and the EZ thickness. This method, based on fitting a 4-parameter idealized profile to observed profiles, was further improved by Hägeli et al. (2000). The analysis showed that the entrainment flux ratio (the ratio of the air entrained from the free troposphere to that entrained from the PBL) is spatially highly variable and that it induces relatively large fluctuations in the observed PBL height. These studies used high temporal and spatial resolution to describe the dynamics of the EZ. Due to the intense exchange between air parcels rising from the CBL and sinking from the free troposphere, the backscatter lidar signal considerably varies with time at the CBL top. The continuous process of mixing at that level suggests using the temporal variability of the backscatter signal (i.e. variance) to retrieve the CBL height.

This study presents backscatter lidar observations of the PBL height with high temporal and altitude resolution. The measurements are divided in two groups of case studies: one group combines five cases of the summer CBL and the other group combines five nighttime winter cases of the stable PBL. Each set of case studies, the convective and the stable, has been selected based on specific requirements on the meteorological conditions and the period of measurements.

The convective cases have been chosen from the summer cases in our dataset, based on air temperature in the range from 25 to 30°C, with no precipitation and during the convective hours, i.e. 1200–1800 UTC. The stable cases have been selected from the winter cases in our dataset, based on temperature in the range from −5 to 1°C, with no precipitation or patchy low-level fog. The measurements have been performed far from the convective hours, i.e. at least 5 h after the sunset.

Martucci et al. (2007) showed the advantage in using the gradient and the variance methods applied to the backscatter lidar signal to retrieve the altitude of both the CBL and NBL heights, as well as the altitude of the (advected) aerosol layers aloft. In the present study these methods are used, along with a data filter based on the averaged PBL height, to retrieve the CBL and NBL heights from the backscatter signal with high temporal and altitude resolution. An automated algorithm implements the two methods to provide the temporal fluctuations of CBL and NBL heights as retrieved from the attenuated atmospheric backscatter coefficient time series. The frequency spectrum of the CBL and NBL height temporal fluctuations is then obtained by applying a Fourier analysis. The frequency spectra show characteristic values for measurements performed in similar meteorological conditions. Distinctive frequencies in each group are interpreted as the frequency of the updraft and downdraft processes for convective cases, and as the frequency of gravity waves occurring at the PBL top for nighttime cases. The observation of gravity waves within and at the top of the PBL has been carried out

until recently mainly using airborne remote sensing instrumentation and only over restricted areas. The emphasis of our study is to investigate the mechanisms of air exchange within the boundary layer using a ground-based lidar and to assess the frequencies of fluctuation of the PBL top during both daytime and nighttime.

2 Site and Conditions for Measurements

The site of measurement is located in the city of Neuchâtel (47.000°N, 6.967°E, 485 m a.s.l.), situated at the south slope of the Jura mountain range (oriented north-east to south-west with highest elevation 1609 m a.s.l.), on the western shore of Lake Neuchâtel (38.3 km long and 8 km wide). The topography determines the local wind circulation and strongly characterizes the PBL during both daytime and nighttime.

During summer days, the convection produces an inflow towards the centre of the thermal initiating the breeze from the lake. When thermals are strong enough, the air entrained from the surroundings may induce a downflow along the Jura slope in opposition to the anabatic circulation (Blumen 1990; McIlveen 1992). Even in moderate convective conditions, the top of a thermal can rise through the first temperature inversion, and then becomes negatively buoyant and sinks back down into the CBL (Scorer 1957; Deardorff 1969; Stull 1973). Small thermals have insufficient energy to reach the CBL top and collapse at some level inside the convective layer. This is confirmed by the fact that the number of thermals decreases with height within the CBL (Greenhut and Khalsa 1987). For this study, we consider only cases of thermals with sufficient energy to reach the CBL top. For such thermals the undiluted air inside their core rises up to the top gradually losing energy; the cooled air sinks, diverging from the thermal's core in columns of downdrafts. The process entrains air from the free troposphere into the CBL resulting in dilution of the aerosol content and growth of its depth. An upward looking, ground-based lidar can probe a sequence of several updrafts and downdrafts carrying different aerosol concentrations (Flamant et al. 1997; Kunz et al. 2002). The backscattered signal is highly sensitive to the aerosol concentration, size and phase, such that large signal echoes return to the lidar receiver when the laser probes updrafts, and vice versa when the target is cleaner air transported in downdrafts from the free troposphere.

In purely convective conditions the updrafts and downdrafts move the air parcels through the CBL on a time scale $t_* = h_C/w_*$, where w_* is the convective velocity scale and h_C is the current CBL height. When the horizontal wind is light, the thermals may stay attached to the hot spot where they form. At higher wind speeds, thermals may form repeatedly over the hot spot and drift downwind. Thermals drift with the average wind, so they may travel at a higher speed and in a somewhat different direction than the surface wind. Downwind moving updrafts and downdrafts appear then at different frequencies through the laser field-of-view (FOV) depending on the horizontal wind speed. In such conditions, at the top of the CBL, two consecutive thermals pass through the lidar FOV in a time $t = (1.5\ h_C)/u$ (Caughey and Palmer 1979; Young 1988a,b,c), where u is the mean horizontal wind speed at the CBL top and h_C is now the thermal mean diameter. The factor 1.5 in the above expression arises from airborne observations of the horizontal thermal distribution (Young 1988a,b,c). Since, in general, $u \gg w_*$, the time for a whole updraft and downdraft cycle to pass through the lidar FOV is $t < t_*$ even if $(1.5\ h_C) > h_C$ (see Fig. 1).

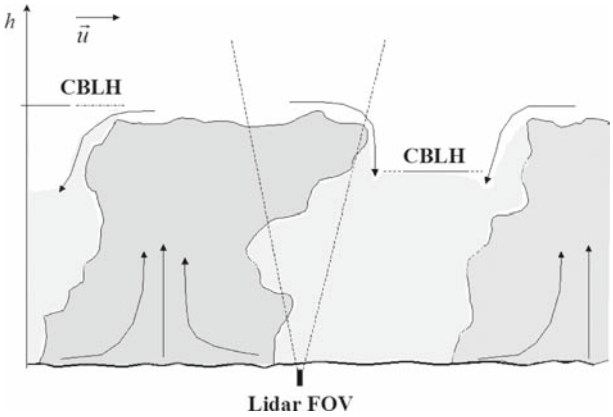

Fig. 1 Idealized vertical cross-section of thermals. The vector $\vec{u}$ is the horizontal wind moving the thermals downstream through the lidar FOV. The CBL height is higher during updrafts than during downdrafts

3 Lidar Instrument and Methods

3.1 The Lidar

The backscatter lidar operated with the second harmonic (532 nm) of a Q-switched Nd-YAG laser, with an emitted output pulse energy of 30 to 45 mJ at a pulse repetition rate of 20 Hz. The receiver has a diameter of 0.25 m. The altitude at which the field-of-view of the receiver completely overlaps the laser beam section is around 400 m. Photomultipliers and a tandem of digital oscilloscopes are used for the data acquisition in analogue mode. Altitude and temporal resolutions of the raw single lidar profile are 6 m and 60 s, respectively. The temporal resolution $\Delta t = 60$ s results from the selected acquisition system mode (1000 shots at 20 Hz), plus the transfer time of the accumulated signal, 10 s. Part of the transmitted laser power is directed to a power monitor and used to normalize the detected atmospheric signal.

The lidar operated within the framework of the EU project EARLINET (Bösenberg and Matthias 2003). The lidar passed the intercomparison campaign and quality assurance procedures carried out in this project (Böckmann et al. 2004). The selected case studies for the presented analysis are part of the dataset collected during the period from May 2000 to February 2003, again within the framework of EARLINET.

3.2 Data Analysis

The power of the signal, $P(h)$, backscattered by an atmospheric layer of thickness Δh (range gate) centred at altitude h can be expressed in the form (Weitkamp 2005):

$$P(h) = P_L K O(h) \frac{A}{h^2} \Delta h \beta(h) T^2(h) + B, \tag{1}$$

where P_L is the emitted optical power, K is the overall optical efficiency of the instrument, $O(h)$ is the overlap function, A is the receiver area and $T(h) = \exp\left\{-\int_0^h \alpha(h')dh'\right\}$ is the round-trip transmission factor. Variables α and β are respectively the extinction (in m^{-1}) and the volume backscattering (in $\mathrm{sr}^{-1}\,\mathrm{m}^{-1}$) coefficients. The term B takes into account the sum of the electronic and optical background noise. The coefficients α and β can be written

as the combination of their aerosol and molecular components, i.e. $\alpha = \alpha_{aer} + \alpha_{mol}$ and $\beta = \beta_{aer} + \beta_{mol}$. Due to the relations $\alpha_{aer}, \beta_{aer} \gg \alpha_{mol}, \beta_{mol}$ valid through the boundary layer, it turns out that $\alpha \approx \alpha_{aer}$ and $\beta \approx \beta_{aer}$. In this study, only altitudes with the receiver FOV completely overlapping the laser beam, i.e., $O(h) \equiv 1$, are taken into account. In the signal processing, the range-corrected signal (*RCS*) is computed as

$$RCS(h) = [P(h) - B]\,h^2, \tag{2}$$

and after corrections, profiles with an initial vertical resolution of 6 m are averaged over two vertical bins (range gates) decreasing the altitude resolution to 12 m.

3.2.1 Gradient Method

The gradient of the signal natural logarithm (Bösenberg and Linné 2002), named *GS*, has the expression:

$$GS(h) = \frac{d}{dh}\ln(RCS) = \frac{d}{dh}\ln(\beta(h)) - 2\alpha(h)\,. \tag{3}$$

Note that the gradient *GS* shows local minima when passing from layers with high aerosol content to layers with low aerosol content and vice versa. For ground-based lidar measurements, the height corresponding to the minimum value of *GS*, h_{GSmin}, indicates the height of the decrease in the aerosol concentration matching the PBL top.

3.2.2 Variance Method

The variance of *RCS* is defined as (Menut et al. 1999):

$$Var(h) = \frac{1}{N}\sum_{k=1}^{k=N}\left(RCS_k(h) - \overline{RCS(h)}\right)^2, \tag{4}$$

where the k index specifies the individual measurements $k = 1, \ldots, N$ occurring during the temporal interval of length N. The optimal value of N depends on the temporal resolution of the measurements and on the duration of a single process of updrafts and downdrafts. The mean value $\overline{RCS(h)}$ is obtained by averaging the single RCS_k profiles over the temporal interval N. The RCS_k profiles have temporal resolution 60 s. The variance *Var* yields the amount of variation of the backscatter signal at a fixed height h with respect to $\overline{RCS(h)}$ during the interval N. The variance shows a local maximum in correspondence to the level at which most of the exchange takes place, i.e. the interface between the PBL and the free troposphere.

4 Signal Processing and Observations

4.1 The Algorithm

Figure 2 sketches the algorithm operations for retrieving the CBL and NBL heights using the gradient and variance profiles. Equations 3 and 4 are re-presented as

$$GS_i(h) = \frac{d}{dh}\ln(RCS_i(h)) = \frac{d}{dh}\ln(\beta(h)) - 2\alpha(h)\,, \tag{5}$$

$$Var(h)_i = \frac{1}{N}\sum_{k=i+1-N/2}^{k=i+N/2}\left(RCS_k(h) - \overline{RCS(h)}_i\right)^2. \tag{6}$$

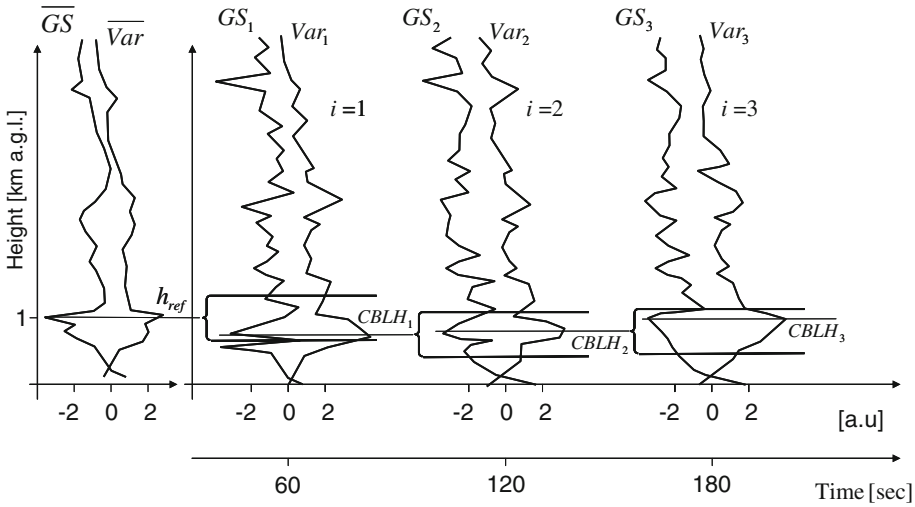

Fig. 2 Synopsis of the lidar algorithm for the retrieval of the PBL height, h_C. Profiles $\overline{GS}$ and $\overline{Var}$ are averaged over the interval $\Delta t_{average} = 30$ min. The reference height h_{ref} is obtained by the averaged profiles and used to initiate the algorithm. Single GS_i and Var_i profiles have temporal and vertical resolutions $\Delta t = 60$ s and $\Delta z = 12$ m

The index *i* in Eqs. 5 and 6 indicates the single successive measurements in the selected period of the case studies. The single GS_i and Var_i profiles provide single evaluations of the PBL height and, combined in a sequence, give its temporal fluctuation. Since the time resolution is 60 s, for 1.5 h of measurement (as used for the case studies), *i* goes from 1 to 90. The moving variance method is applied to each *i*-profile within the temporal interval $[i - N/2, i + N/2]$. For 90 min of measurements, *i* goes from 5 to 85. The parameter *N* is the length of the *k*-index and has here the value $N = 10$. Each $Var(h)_i$ profile gives the variability of the backscatter signal at altitude *h*, during the interval of *N* successive measurements.

Further, the algorithm computes the mean $\overline{GS}$ and $\overline{Var}$ values from single GS_i and Var_i profiles averaged over 30 min (*i* goes from 1 to 30). The applied altitude and time averaging on RCS_i profiles decreases the shot noise contribution by a factor $E = \left(n_p n_b\right)^{0.5}$, where n_p and n_b are respectively the number of single profiles (*i*-index) and the number of range bins (gates) in the altitude profile used for averaging. In our case, $n_p = 30$ and $n_b = 2$, so $E = 8$. The resulting reduction of false peaks makes the detection of the $\overline{GS}$ minimum and $\overline{Var}$ maximum altitudes easier and provides the actual 30-min average PBL height.

At its first step the algorithm detects, starting from the ground level, the heights of the first minimum and maximum of $\overline{GS}$ and $\overline{Var}$, respectively. The mean value between the two heights is the reference height, h_{ref}. The related error is $\sigma_{ref} = \sqrt{\sigma^2_{\overline{GS}} + \sigma^2_{\overline{Var}}}$, where the standard deviations of $\overline{GS}$ and $\overline{Var}$ are calculated over the 30- min average at the reference heights and are supposed to be statistically independent.

After having determined $h_{ref}(i = 1)$, a range of altitudes $h_j \in [0.85(h_{ref} - \sigma_{ref}) - 1.15(h_{ref} + \sigma_{ref})]$ limits the vertical region in which to search for the principal minimum and maximum of GS_1 and Var_1, respectively. The mean value between the heights of the GS_1 minimum and of the Var_1 maximum found in that interval is the first CBL (NBL) top computed altitude ($h_{C,1}$). The uncertainty on the determined CBL (NBL)

top value is equal to the standard deviation of the other possible heights, which have been finally rejected by the algorithm.

For $2 \leq i \leq 30$, the algorithm determines, in the new range of altitudes $[0.85(h_{C,i-1} - \sigma_{h_{C,i-1}}) - 1.15(h_{C,i-1} + \sigma_{h_{C,i-1}})]$, a new value of the CBL height at each i-step (see Fig. 2). For $i = 31$, the algorithm computes two new $\overline{GS}$ and $\overline{Var}$ profiles averaged over the successive time interval $i \in [31 - 60]$. The algorithm performs the same process as for the first 30 i-steps with a new initial h_{ref} value. The algorithm is built in groups of 30 steps each until the end of the dataset. The algorithm output is then a time series of CBL (NBL) heights each with related uncertainty.

4.2 Fourier Analysis

For a time-domain signal, as with the PBL (CBL or NBL) top time series, the power spectral density describes how the power of the signal is distributed in frequency. So, for each case study of convective and stable PBL evolution presented in Sects. 4.3 and 4.4, a fast Fourier transform (FFT) was applied to the PBL height temporal fluctuation to evaluate its frequency components. Before applying the FFT, the linear trend of each PBL height time series has been removed.

The precision of the FFT algorithm being very high, the only source of uncertainties relates to the PBL height determination. The uncertainties (in terms of error bars) of each PBL top time-series point are regarded as white (random) noise, which is superimposed on the PBL height signal, and whose amplitude is equal to that of the error bars. The Fourier transform is then applied to both the error-free and noise-containing signals to determine the uncertainty in the frequency spectra. The rate of sampling, imposed by the acquisition system, is $f_s = 16$ mHz; the Nyquist frequency is then $f_{Nyq} = 0.5\, f_s = 8$ mHz. The useful part of the spectrum is limited to the frequency range between 0 and f_{Nyq} Hz.

The spectra in the further sections are analyzed based only on the principal frequency components present in each spectrum, i.e. the components having maximum power amplitude.

4.3 Observations: Convective Case

4.3.1 Case Studies

The convective dataset includes five case studies of CBL temporal fluctuation. Table 1 presents the initial and final time of measurements—all measurements have a duration of 1.5 h—and parameters characterizing the CBL during the period of observation. The wind speed values at the CBL top are derived from 1200 UTC radiosoundings performed at the MeteoSwiss aerological station in Payerne (20 km south of Neuchâtel), while the values of temperature and horizontal wind speed at 30 m come from the MeteoSwiss meteorological station in Neuchâtel. In Martucci et al. (2007), lidar measurements at the Neuchâtel site have been compared with the vertical temperature profiles recorded by radiosondes launched from Payerne. A careful analysis of the possible sources of uncertainty was carried out through this study, demonstrating that the two sites can be compared despite their distance. Figure 3 shows the *RCS* time series with superimposed temporal fluctuations of CBL height and error bars (white curve). The Brunt–Väisäillä frequency F is defined as

$$F^2 = g \frac{d \ln \theta}{dh}, \tag{7}$$

Date	Period of measurement (UTC)	T (°C)	u_{30m} (m s^{-1})	$u_{\overline{h_C}}$ (m s^{-1})	$\overline{h_C}$ (m)
22 Aug 2001	1230–1400	24.5	4.2	13	1035
23 Aug 2001	1230–1400	24	1.8	2	660
22 Jun 2002	1330–1500	28.5	2.5	20	2500
15 Aug 2002	1700–1830	25	3	3.5	1450
30 Aug 2002	1240–1410	24.5	3	9.5	1440

The meteorological data are from MeteoSwiss (regular measurements at the Neuchâtel meteorological station and 12 h-UTC radiosoundings from Payerne aerological station, 20-km south of Neuchâtel). T is the temperature at ground, u_{30m} and $u_{\overline{h_C}}$ are the horizontal wind speed at 30 m and at the CBL averaged height, respectively, h_C is the CBL averaged height over the period of measurement

where g is the gravitational acceleration and θ the potential temperature. For all the analyzed cases, at the altitude corresponding to the mean CBL top, the Brunt–Väisäillä frequency F ranges between 9 and 16 mHz. It is hence larger than f_{Nyq} and will not be considered for interpretation of spectra shown in Fig. 4.

In convective conditions with small horizontal wind speed, the updraft and downdraft process is responsible for the principal variations of the CBL top. Analyzing each spectrum separately, there exist no cases in which the uncertainty amplitude could prevent a unique choice of the principal peak. The value of the main component f in each spectrum does not differ from case to case as would be expected if conditions were purely convective. Actually, in purely convective conditions, for comparable values of w_*, the time $t_* = h_C/w_*$ is expected to increase for increasing h_C values; the same holds for f^{-1}. As an example, the two cases for 23 August 2001 and 22 June 2002 have significantly different $\overline{h_C}$ values, 660 and 2500 m, respectively. If conditions were purely convective, a higher frequency should have been observed on 23 August 2001 with the shallow CBL. On the contrary, a higher value of f is obtained, corresponding to a deeper CBL. The apparent inconsistency can be explained by considering the horizontal wind u at the level of the CBL top that moves thermals downstream at the time rate $t = 1.5\,h_C/u$.

Values of f are shown in spectra in Fig. 4: on 23 August 2001, a higher frequency corresponds to a shallow CBL (660 m) and vice versa on 22 August 2001 with a deeper CBL (1035 m). On 22 August 2001, the horizontal component of the wind speed is almost constant through the CBL whereas it increases with altitude on 23 August 2001. On 22 June 2002, the horizontal wind at the CBL top had a value of 20 m s^{-1}, considerably higher than for the other cases. With respect to its CBL height (2500 m), the main spectral component f in panel (c) has a relatively high value ($\approx$4 mHz) especially when compared to the principal components in the other spectra. This value of f is likely determined by the process having the time period $t = 1.5\,h_C/u$. The last two cases, 15 and 30 August 2002, have similar CBL heights, temperatures and 30-m wind speed values. Both spectra have main components at about 3 mHz. It is then likely that the two cases are dominated by purely convective conditions.

4.3.2 Comparison of Individual Spectra

To establish whether the five independent spectra share a common feature, a product of the power levels in each frequency of the individual spectra is obtained (dot product); then the fifth root of the product is taken to retrieve the power of the spectrum of the common features.

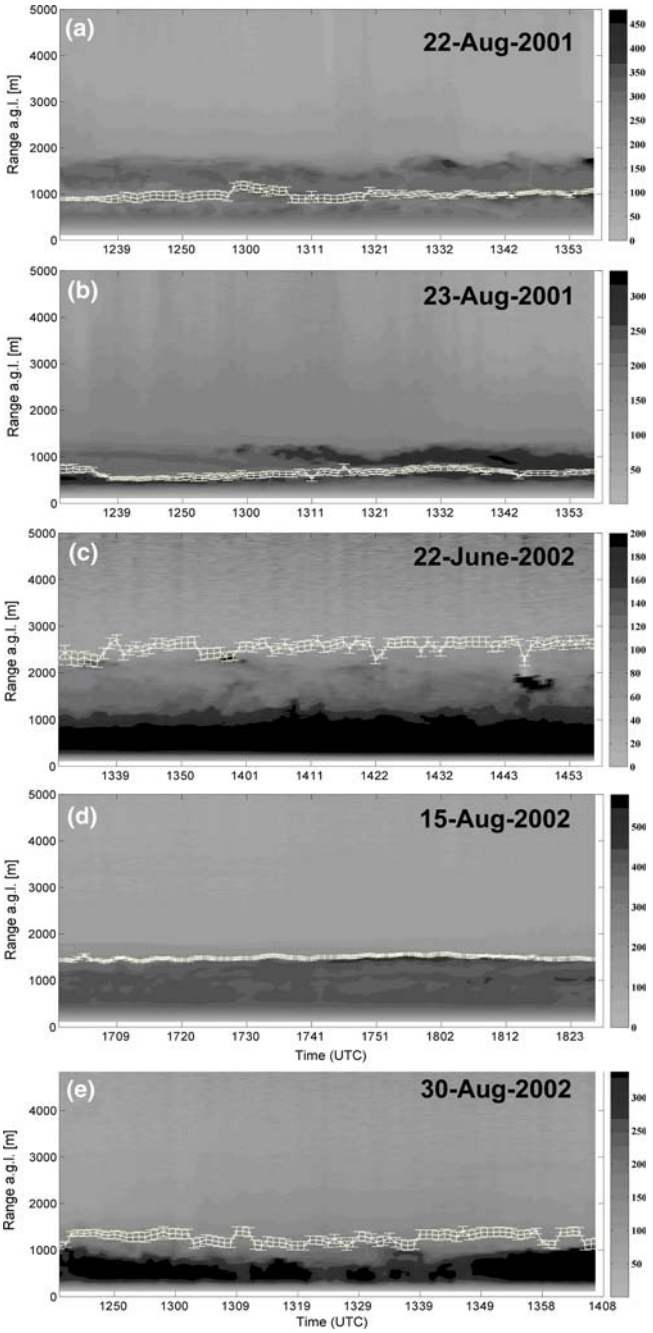

Fig. 3 **a–e** Five convective cases of CBL height temporal fluctuation (*white curve with error bars*) and RCS time series. *Darker regions* correspond to higher aerosol backscatter. The duration of measurements is 1.5 h for each case

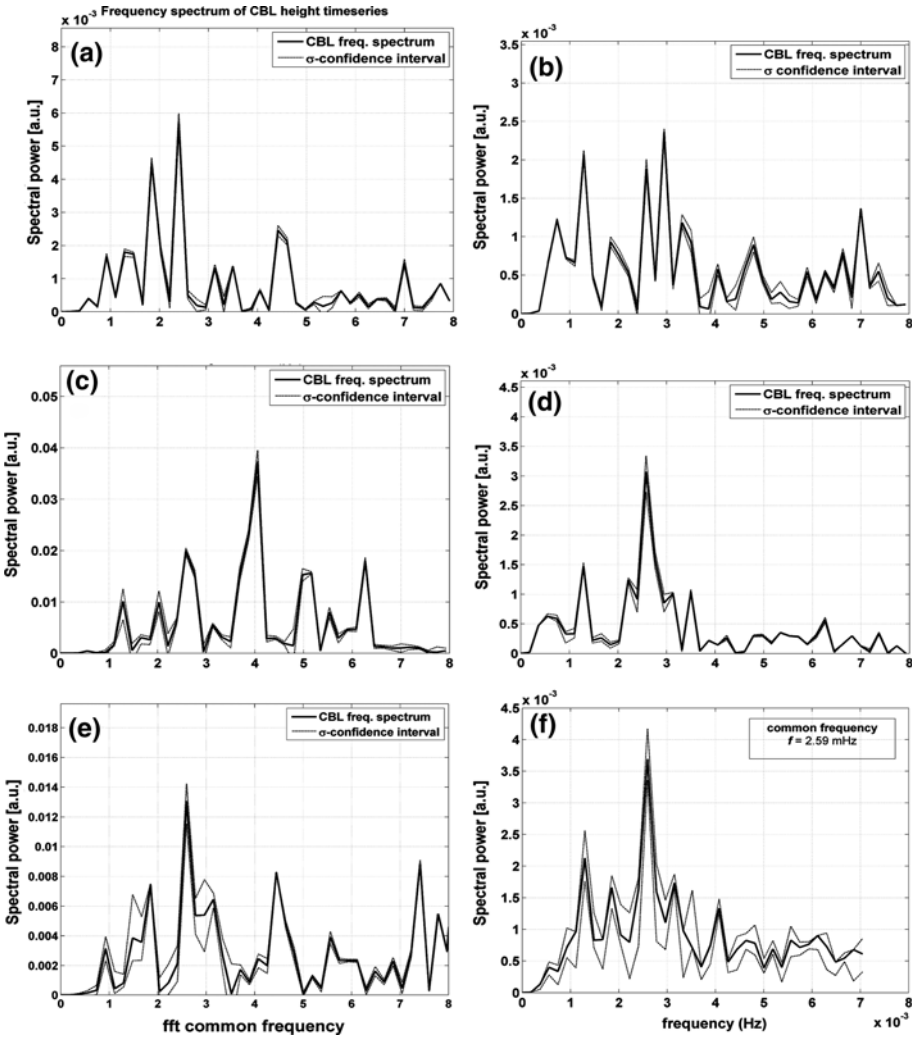

Fig. 4 **a**–**e** Power spectra computed from the temporal fluctuation of the CBL height in Fig. 3. The 1σ-uncertainty intervals are shown with *dashed lines* above and below the *solid curve*. **f** shows the fifth root of the dot product of the above five spectra. The common frequency is 2.6 mHz

The resulting power spectrum is equivalent to that of the cross-correlation of the corresponding PBL height fluctuations in the time domain. The result of this operation is shown in Fig. 4f. The main spectral component is $f_{common} = 2.6$ mHz. The presence of a common frequency in all spectra indicates that the fluctuation f_{common} depends on common CBL dynamics. It is to be noticed that the wind direction is from the south-east in all studied cases. Indeed, two different measurements of the wind direction were performed, one at the MeteoSwiss meteorological station at Chasseral (1599 m a.s.l, 16 km north-east of Neuchâtel) and one at Neuchâtel (485 m a.s.l.). During the period of lidar observations, both stations provided the same direction of the horizontal wind for the five case studies (i.e. from the south-east).

An interpretation of f_{common} is that this frequency is determined by the combined effects of topography and wind direction on the temporal fluctuation of the CBL top. Before reaching

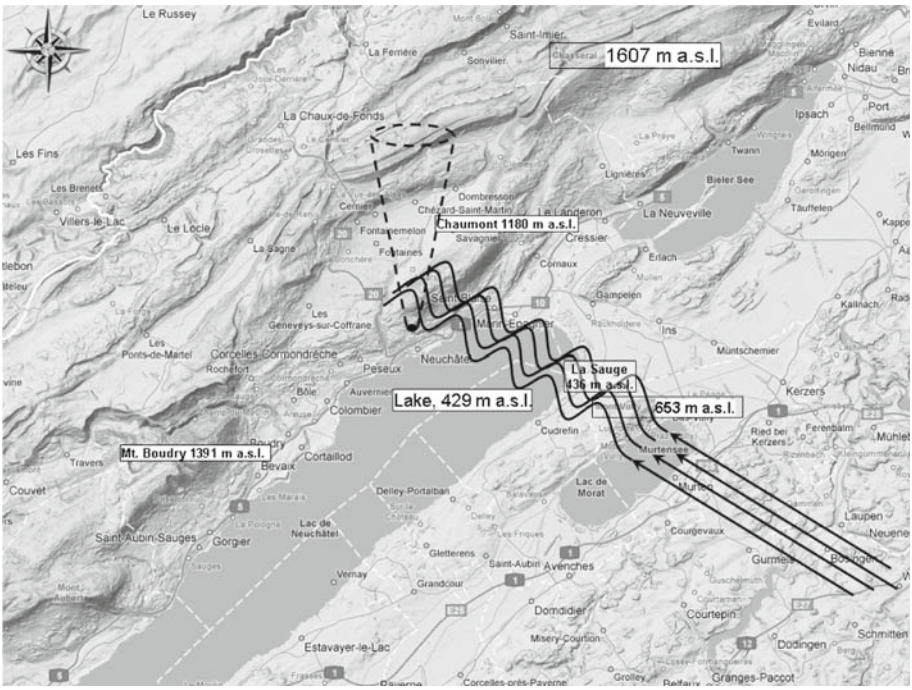

Fig. 5 System of CBL-trapped lee waves developing on the lee side of Mt. Vully (653 m a.s.l.) and travelling towards the city of Neuchâtel in an overall south-eastern flow

Neuchâtel, air masses from south-east have to pass over a low-elevation hill range set between Lake Neuchâtel and Lake Morat and extending parallel to the Jura axis for about 8 km. The highest peak is Mt. Vully (653 m a.s.l., 11 km south-east of Neuchâtel), 260 m above the level of both lakes (see Fig. 5). Due to the small altitude of the hill range, the Froude number (Stull 1988, Eqs. 14.2.3a–b) is $Fr \approx 1$, even for weak winds. Lee waves may then form vertically above or horizontally downwind of Mt. Vully.

In linear theory, the Scorer parameter $l(h)$ is defined as,

$$l^2(h) = \frac{F^2}{U^2} - \left(\frac{\partial^2 U}{\partial^2 h}\right)\frac{1}{U}, \tag{8}$$

where $l(h)$ depends on altitude h, wind speed U and Brunt–Väisäillä frequency F, and usually strongly decreases with height through the CBL. Above the level of the first temperature inversion, $l(h)$ is nearly constant with height. Such conditions are favourable for vertically propagating mountain waves. Since the hill range altitude is below the level of the first temperature inversion for all studied cases, waves forming beyond the hill range become trapped inside the CBL and propagate towards the Neuchâtel site.

For a ground-based backscatter lidar, stationary trapped lee waves represent a still system that does not contribute to CBL-top temporal fluctuations. Exceptions to the system steady state are two: (i) Trapped lee waves may evolve over time as a non-stationary wave system (Caccia et al. 1997; Ralph et al. 1997; Nance and Durran 1997, 1998). Actually, time variations of the group velocity and wavelength may occur on the lee side of the hill as the parameters in Eq. 8 change upstream. (ii) There is an expected wave reflection at the Jura southern mountain side. Since the incident angle is not 90°, there will be a superposition of

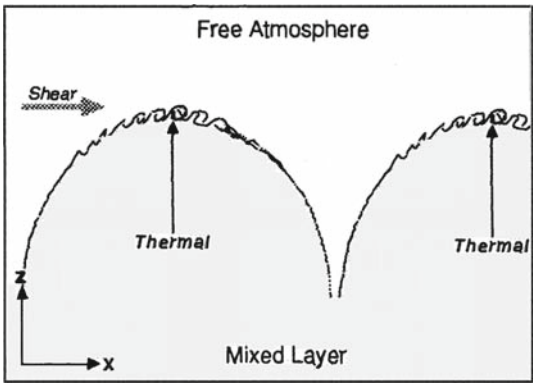

Fig. 6 Small-scale KH waves forming at the top of overshooting thermals due to height-increasing shears and stability (Rayment and Readings 1974; Stull 1988)

forward and backward waves resulting in a pattern of constructive and destructive interference. Based on these facts, the wave field above Neuchâtel cannot be regarded as stationary during the period of lidar observation. The frequency f_{common} in Fig. 4f may be considered as determined by the non-stationary component of the wave field.

Another way to interpret the existence of the shared frequency f_{common} is to analyze the wave dynamics on a smaller scale. Kelvin–Helmholtz (KH) waves can exist in the entrainment zone on different scales. At the largest scale KH waves arise from the shear between sub- and nearly-geostrophic winds, respectively, inside and above the CBL. At the smaller scale, KH waves may form along the top boundary of overshooting thermals and may cause the CBL top to be fluctuating (Rayment and Readings 1974). The tops of thermals are marked by a sharp interface with free tropospheric air. The abrupt gradient between two different air parcels can lead to very strong shear and a statically stable lapse rate across a distance of a few metres, The KH waves that may form in such a situation are typically short wavelength and evolve rapidly over time during the ascent phase of thermals through the EZ (see the outline in Fig. 6). The whole process of wave formation, break-up and decay in turbulence takes a few minutes, with a wave period comparable to that determined by f_{common}.

4.4 Observations: Non-Convective Case

Temporal fluctuations of the PBL height occur also in stable conditions, where a number of factors such as inertial oscillations or drainage flows may activate turbulence across the nocturnal boundary layer. A superposition of more than one factor usually results in a complicated NBL structure. In this section we provide qualitative interpretations to the oscillations occurring at the NBL top, focusing on the effects of wind shear and gravity waves.

4.4.1 Case Studies

Five winter, stable, nocturnal cases of PBL temporal fluctuation are studied. Their *RCS* time series with a superimposed temporal fluctuation of the NBL top and related error bars (white curve) are shown in Fig. 7. All measurements were performed a few hours after the sunset in order to avoid or limit the possible presence of residual convection. Small altitude variations, always around the mean NBL height values, can be noticed. The periods of the measurements and the relevant meteorological parameters, along with the wind speed at 30 m, are reported in Table 2. The wind speed at the level of the mean NBL height comes from the midnight

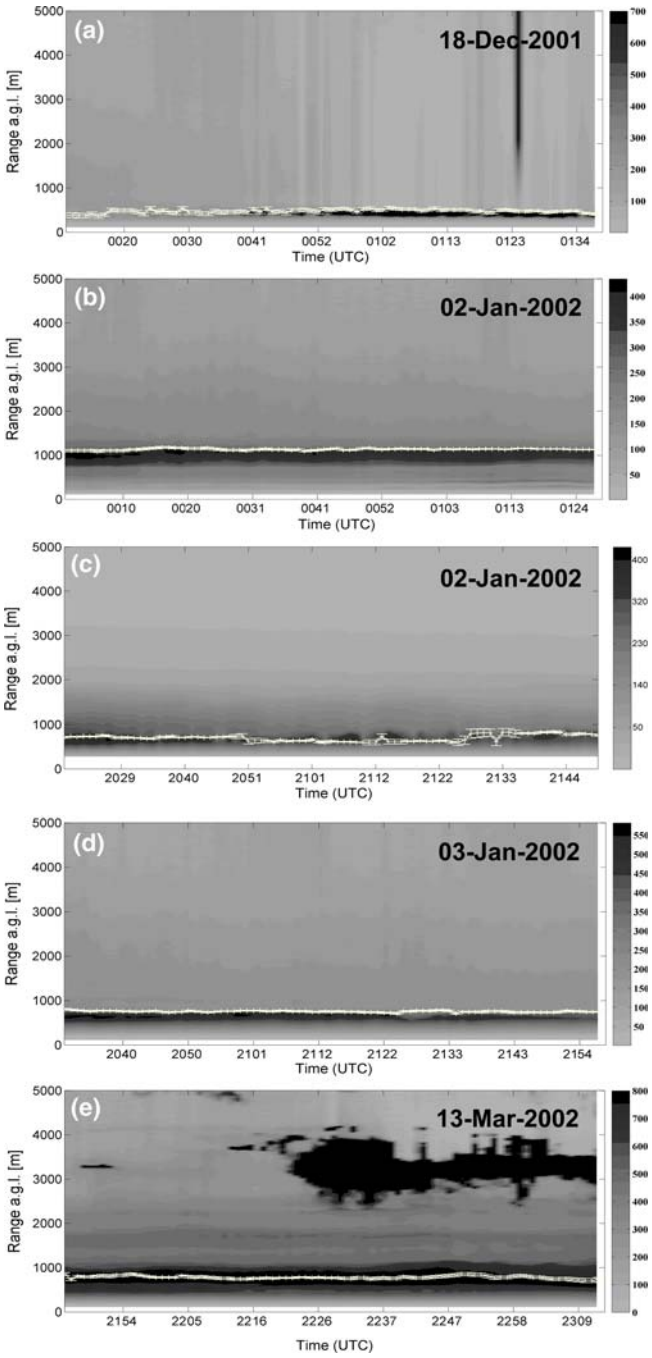

Fig. 7 **a**–**e** Five non-convective cases of nocturnal stable PBL height fluctuation (*white curve with error bars*) and RCS time series. *Darker regions* correspond to higher aerosol backscatter. Measurement duration is 1.5 h for each case

Table 2 Physical and meteorological parameters characterizing the NBL during five stable case studies

Date	Period of measurement (UTC)	T (°C)	u_{30m} ($\mathrm{m\,s^{-1}}$)	$u_{\overline{h_N}}$ ($\mathrm{m\,s^{-1}}$)	$\overline{h_N}$ (m)
18 Dec 2001	0010–0140	−2.5	3.5	16	430
02 Jan 2002	0000–0130	−5	1.2	13	1130
02 Jan 2002	2020–2150	−3	1	9	612
03 Jan 2002	2030–2200	−2.7	2	9	747
13 Mar 2002	2145–2315	1.1	0.5	2	776

See Table 1 for a detailed description of the parameters

radiosoundings made at the MeteoSwiss aerological station in Payerne. The wind speed inside the NBL is between 0.5 and 3.5 $\mathrm{m\,s^{-1}}$. In the five cases, this is in good agreement with the expected range for a katabatic wind (Stull 1988, p. 535). During all cases, the wind direction periodically changes, between north-east and north-west. It should be noted that the katabatic flow from the Jura slope is a north-westerly wind. In the presence of a decoupled flow with higher level flow from the north-east, it is likely to observe the wind direction swinging between north-west and north-east. At higher levels the wind speed increases in all cases except for the case on 13 March 2002 when the wind speed remains almost constant through the NBL.

Figure 8 presents the spectra as obtained by Fourier transform, i.e. applying the FFT to the temporal fluctuation of the NBL height. The uncertainty intervals (plotted with dashed lines above and below the solid curve) have been determined using the same procedure as for the convective cases. From all cases in this group, Fig. 8a presents a case fluctuation of a particularly shallow NBL with top around 500 m. The other cases present the NBL with tops around 700–800 m. During nighttime, internal waves with frequencies lower than the Brunt–Väisälä frequency are trapped within the NBL resulting in waves propagating horizontally through the NBL and at the level of the NBL top. Kelvin–Helmholtz waves can be generated by the wind shear during night: the laminar flows become unstable under the action of the wind shear leading to KH-wave formation at the levels where the (gradient) Richardson number Ri becomes smaller than a certain critical value R_c, where

$$Ri = \frac{\dfrac{g}{\theta_v}\dfrac{\partial \theta_v}{\partial z}}{\left[\left(\dfrac{\partial U}{\partial z}\right) + \left(\dfrac{\partial V}{\partial z}\right)\right]^2}, \tag{9}$$

and θ_v is the virtual potential temperature, T_v is the virtual absolute temperature, z the altitude, g the gravitational acceleration and (U, V) are the wind components towards the east and the north. The levels at which KH waves may form are the *critical levels*, and at such levels Ri is smaller than $R_c = 0.25$ (Stull 1988, p. 176). Payerne radiosoundings provide a spot measurement of the wind direction around 0000 UTC. In all cases the profiles show strong shear at the altitude of the NBL top. The local maximum in the wind shear supports the hypothesis of KH waves present at the top of NBL. A qualitative analysis of each spectrum shows that an isolated, well-pronounced peak of frequency is present only on 13 March 2002.

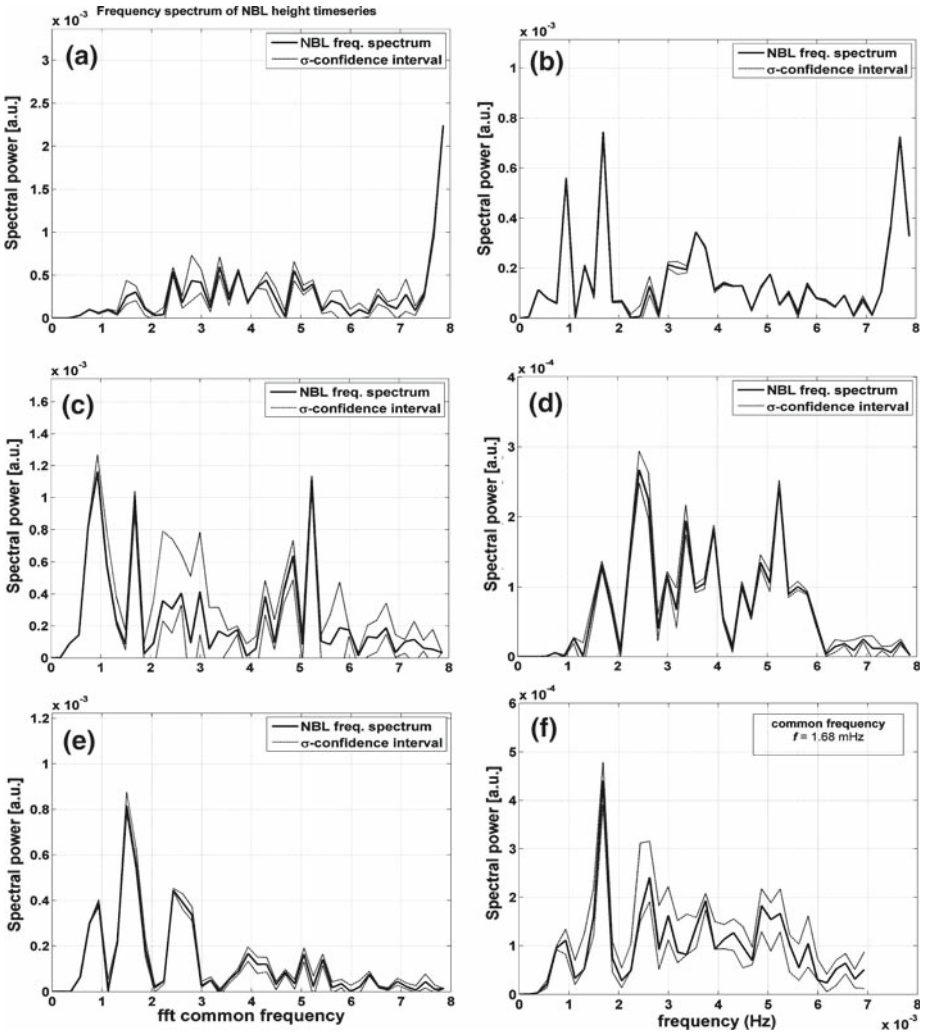

Fig. 8 **a**–**e** Power spectra computed from the temporal fluctuation of the NBL height in Fig. 7. The 1σ-uncertainty intervals are shown with *dashed lines* above and below the *solid curve*. **f** shows the fifth root of the dot product of the above five spectra. The common frequency is 1.68 mHz

4.4.2 Comparison of Individual Spectra

The dot-product method described above (see Sect. 4.3.2) is applied to the stable NBL cases presented in Fig. 8a–e. The resulting power spectrum is shown in Fig. 8f. One common frequency component emerges clearly, indicating that it is present in each one of the individual spectra. This common frequency is $f_{common} = 1.68$ mHz, a value closely corresponding to the principal components in each spectrum. When compared to the convective cases, the value of f_{common} for the stable cases is shifted backward in the frequency domain. The frequency f_{common} denotes a process taking place during each of the five cases without being necessarily the dominant one. The KH wave formation may occur during all the presented

cases as induced by the strong shear at the NBL top. Then it is very likely that f_{common} is due to KH waves passing through the lidar field-of-view.

5 Conclusion

This study investigates the frequencies that characterize the temporal fluctuations of the PBL top in convective and stable conditions. A backscatter lidar has been used to remotely sense the boundary-layer structure. The lidar backscatter signal is processed by a synergetic gradient and variance method implemented into an automated algorithm able to detect the PBL height at high temporal and vertical resolution.

Two groups of cases have been analysed, one group that includes five daytime convective PBL observations and one that combines five cases of stable nighttime PBL. For both groups, the altitude variations of the PBL top were studied for each case over a period of 90 min. To detect the main frequency components, a fast Fourier transform was applied to the temporal evolutions of the PBL tops during the period of measurement. The temporal and vertical resolutions of the lidar measurements were 60 s and 12 m. The analysis of each frequency spectrum in the two groups showed that more than one process contributes to the fluctuations in the PBL tops. A common frequency was found for each group and this differs slightly for the convective and stable cases. For convective cases, updraft and downdraft processes explained most of the fluctuations in the frequency spectra. Interpretation of the common frequency, f_{common}, draws on the combined effect of (i) the local topography, and (ii) thermals dynamics: (i) A system of non-stationary trapped lee waves engendered by a south-easterly flow can form on the lee side of Mt. Vully (east of Neuchâtel) and propagate towards the Neuchâtel site. Variations in the wave wavelength and group velocity upstream of Mt. Vully can determine a non-steady fluctuation in the CBL top with frequency f_{common}. (ii) Thermals rising through the entrainment zone experience a strong gradient of static stability and wind shear generating a system of short wavelength KH waves on their top surfaces.

The second group combines stable nocturnal PBL cases, with similar meteorological conditions. A decoupled flow at the NBL top occurred for all stable cases potentially leading to shear instability and KH wave formation. The KH waves have their onset at the levels where Ri is smaller than $R_c = 0.25$ a condition likely achieved during all the stable cases. This process has characteristic frequency of the order of f_{common} and can then provide the interpretation to it.

Our study outlines an effective method based on Fourier analysis of lidar-detected PBL-top time series for investigating fast processes occurring inside and at the top of the PBL. The method allows description of the mechanisms of air exchange between the boundary layer and the free troposphere aloft as well as the mixing processes within the PBL. Depending on the conditions, the ground-based lidar observations may be either complementary or a substitute to aircraft and satellite observations (Alpers and Stilke 1996; Lane et al. 2000; Doyle and Smith 2003). The former involves a limited number of passages over the probed atmospheric region, while the latter requires the presence of clouds in order to detect waves. Realistically, such a lidar method requires observation of the exchange processes between the PBL and the free troposphere over a long period of measurements and in cloud-free conditions. In view of this, and as a further step, it is desirable to validate a number of representative cases for this type of wave observation with reference to the traditionally accepted methods.

Acknowledgments This study was supported by Swiss National Science Foundation Subsidy 2000-067051.01/1. The measurements were performed in the frame of EC project EARLINET, supported by Swiss OFES Contract 99.0650-1. The authors greatly acknowledge MeteoSwiss for observations from the Payerne aerological station and the Neuchâtel surface meteorologica l station.

References

Alpers W, Stilke G (1996) Observation of nonlinear wave disturbance in the marine atmosphere by the synthetic aperture radar aboard the ERS-1 satellite. J Geophys Res 101(C3):6513–6525

Beyrich F, Gryning SE (1997) Estimation of the entrainment zone depth in a shallow convective boundary layer from sodar data. J Appl Meteorol 37:255–268

Blumen W (ed) (1990) Atmospheric processes over complex terrain. American Meteorological Society, Boston, 394 pp

Böckmann C, Wandinger U, Ansmann A, Bösenberg J et al (2004) Aerosol lidar intercomparison in the framework of EARLINET: Part II-aerosol backscatter algorithms. Appl Opt 43:977–989

Bösenberg J, Linné H (2002) Laser remote sensing of the planetary boundary layer. Meteorol Z 11:233–240

Bösenberg J, Matthias V (2003) EARLINET: European Aerosol Research Lidar Network to establish an aerosol climatology. Final report for the period of February 2000 to February 2003 (contract EVRI-CTI999-40003), 62 pp

Caccia JL, Benech B, Klaus V (1997) Space–time description of nonstationary trapped lee waves using ST radars, aircraft and constant volume balloons during the PYREX experiment. J Atmos Sci 54:1821–1833

Caughey SJ, Palmer SG (1979) Some aspects of turbulence structure through the depth of the convective boundary layer. Q J Roy Meteorol Soc 105:811–827

De Wekker SFJ, Kossmann M, Fielder F (1997) Observations Of daytime mixed layer heights over mountainous terrain during the TRACT field campaign. In: Proceedings of the 12th AMS symposium on boundary layers and turbulence, Vancouver, BC, Canada. American Meteorological Society, Boston, pp 498–499

Deardorff JW (1969) Numerical study of heat transport by internal gravity waves above a growing unstable layer. Phys Fluids Suppl II 12:184–194

Doyle JD, Smith RB (2003) Mountain waves over the Hohe Tauern: influence of upstream diabatic effects. Q J Roy Meteorol Soc 129:799–824

Flamant C, Pelon J, Flamant PH, Durand P (1997) Lidar determination of the entrainment zone thikness at the top of the unstable marine atmospheric boundary layer. Boundary-Layer Meteorol 83:247–284

Garratt JR (1992) The atmospheric boundary layer. Cambridge University Press, UK, 316 pp

Greenhut GK, Khalsa SJS (1987) Convective elements in the marine atmospheric boundary layer. Part I: Conditional sampling statistics. J Appl Meteorol 26:813–823

Hägeli P (1998) Evaluation of a new technique for extracting mixed layer depth and entrainment zone thickness from lidar backscatter profiles. Diploma thesis at the Dept. of Geography of the Swiss Federal Institute of Technology ETHZ

Hägeli P, Steyn DG, Strawbridge KB (2000) Spatial and temporal variability of mixed-layer depth and entrainment zone thickness. Boundary-Layer Meteorol 97:47–71

Hennemuth B, Lammert A (2006) Determination of the atmospheric boundary layer height from radiosonde and lidar backscatter. Boundary-Layer Meteorol 120:181–200

Kunz GJ, De Leeue G, Becker E, O'Dowd CD (2002) Lidar observations of atmospheric boundary layer stucture and sea spray aerosol plumes generation and transport at Mace Head, Ireland. (PARFORCE experiment). J Geophys Res 107(D19):8106. doi:10.1029/2001JD001240

Lammert A, Bösenberg J (2006) Determination of the convective boundary layer height with laser remote sensing. Boundary-Layer Meteorol 119:158–170

Lane TP, Reeder MJ, Morton BR, Clark TL (2000) Observations and numerical modelling of mountain waves over the Southern Alps of New Zealand. Q J R Meteorol Soc 126:2765–2788

Martucci G, Matthey R, Mitev V, Richner H (2007) Comparison between backscatter lidar and radiosonde measurements of the diurnal and nocturnal stratification in the lower troposphere. J Atmos Ocean Technol 24:1231–1244

McIlveen R (1992) Fundamentals of weather and climate. Chapman & Hall, UK, 497 pp

Menut L, Flamant C, Pelon J, Flamant PH (1999) Urban boundary layer height determination from lidar measurements over the Paris area. Appl Opt 38:945–954

Nance L, Durran D (1997) A modeling study of nonstationary trapped mountain lee waves. Part I: Mean flow variability. J Atmos Sci 54:2275–2291

Nance L, Durran D (1998) A modeling study of nonstationary trapped mountain lee waves. Part II: Nonlinearity. J Atmos Sci 55:1429–1445

Neu U, Künzle T, Wanner H (1994) On the relation between ozone storage in the residual layer and the daily variation in near-surface ozone concentration—a case study. Boundary-Layer Meteorol 69:221–247

Ralph FM, Neiman PJ, Keller TL, Levinson D, Fedor L (1997) Observations, simulations, and analysis of nonstationary trapped lee waves. J Atmos Sci 54:1308–1333

Rampanelli G, Zardi D (2004) A method to determine the capping inversion of the convective boundary layer. J Appl Meteorol 43:925–933

Rayment R, Readings CJ (1974) A case study of the structure and energetics of an inversion. Q J Roy Meteorol Soc 100:221–233

Scorer RS (1957) Experiments on convection of isolated masses of buoyant fluid. J Fluid Mech 2:583–594

Sicard M, Perez C, Rocadenbosch F, Baldasano J, Garcıa-Vizcaino D (2006) Mixed-layer depth determination in the Barcelona Coastal Area from regular lidar measurements: methods, results and limitations. Boundary-Layer Meteorol 119:135–157

Siebert P, Beyrich F, Gryning SE, Joffre S, Rasmussen A, Tercier Ph (2001) Review and intercomparison of operational methods for the determination of the mixing height. Atmos Environ 34:1001–1027

Steyn DG, Baldi M, Hoff RM (1998) A new technique to derive mixed layer depth and entrainment zone thickness from lidar profiles. In: Abstracts of papers of the 19th international laser radar conference (ILRC), Annapolis, USA, 6–10 July 1998, pp 461–464

Steyn DG, Baldi M, Hoff RM (1999) The detection of mixed layer depth and entrainment zone thickness from lidar backscatter profiles. J Atmos Ocean Technol 16:953–959

Stull RB (1973) Inversion rise model based on penetrative convection. J Atmos Sci 30:1092–1099

Stull RB (1988) An introduction to boundary layer meteorology. Kluwer Academic Publishers, Dordrecht, 666 pp

Weitkamp C (2005) Lidar: range-resolved optical remote sensing of the atmosphere. Springer series of optical sciences, vol 102, 460 pp

Wiegner M, Emeis S, Freudenthaler V, Heese B, Junkermann W, Münkel Ch, Schäfer K, Seefeldner M, Vogt S (2006) Mixing layer height over Munich, Germany: variability and comparisons of different methodologies. J Geophys Res 111:D13201. doi:10.1029JD006593

Young GS (1988a) Convection in the atmospheric boundary layer. Earth Sci Rev 25:179–198

Young GS (1988b) Turbulence structure of the convective boundary layer I: variability of normalized turbulence statistics. J Atmos Sci 45:719–726

Young GS (1988c) Turbulence structure of the convective boundary layer II: PHOENIX 78 aircraft observations of thermals and their environment. J Atmos Sci 45:727–735

Zampieri M, Malguzzi P, Buzzi A (2005) Sensitivity of quantitative precipitation forecast to boundary layer parameterization: a flash flood case study in the Western Mediterranean. Nat Hazards Earth Syst Sci 5:603–612